Drosophila Ncd reveals an evolutionarily conserved powerstroke mechanism for homodimeric and heterodimeric kinesin-14s

Pengwei Zhang[a,1], Wei Dai[b,1], Juergen Hahn[b,c,2], and Susan P. Gilbert[a,2]

[a]Department of Biological Sciences, [b]Department of Chemical & Biological Engineering, and [c]Department of Biomedical Engineering, Center for Biotechnology and Interdisciplinary Studies, Rensselaer Polytechnic Institute, Troy, NY 12180

Edited by Thomas D. Pollard, Yale University, New Haven, CT, and approved April 14, 2015 (received for review March 21, 2015)

Drosophila melanogaster **kinesin-14 Ncd cross-links parallel microtubules at the spindle poles and antiparallel microtubules within the spindle midzone to play roles in bipolar spindle assembly and proper chromosome distribution. As observed for *Saccharomyces cerevisiae* kinesin-14 Kar3Vik1 and Kar3Cik1, Ncd binds adjacent microtubule protofilaments in a novel microtubule binding configuration and uses an ATP-promoted powerstroke mechanism. The hypothesis tested here is that Kar3Vik1 and Kar3Cik1, as well as Ncd, use a common ATPase mechanism for force generation even though the microtubule interactions for both Ncd heads are modulated by nucleotide state. The presteady-state kinetics and computational modeling establish an ATPase mechanism for a powerstroke model of Ncd that is very similar to those determined for Kar3Vik1 and Kar3Cik1, although these heterodimers have one Kar3 catalytic motor domain and a Vik1/Cik1 partner motor homology domain whose interactions with microtubules are not modulated by nucleotide state but by strain. The results indicate that both Ncd motor heads bind the microtubule lattice; two ATP binding and hydrolysis events are required for each powerstroke; and a slow step occurs after microtubule collision and before the ATP-promoted powerstroke. Note that unlike conventional myosin-II or other processive molecular motors, Ncd requires two ATP turnovers rather than one for a single powerstroke-driven displacement or step. These results are significant because all metazoan kinesin-14s are homodimers, and the results presented show that despite their structural and functional differences, the heterodimeric and homodimeric kinesin-14s share a common evolutionary structural and mechanochemical mechanism for force generation.**

presteady-state kinetics | dynamic modeling | microtubules

In the early stages of mitosis and meiosis, the bipolar metaphase spindle must be established, and kinesin-14 molecular motors play key roles in this process (1–4). In contrast to the microtubule (MT) plus-end directed processive kinesins, kinesin-14s are not processive as single molecules; they promote MT minus-end-directed force and use an ATP-promoted powerstroke to cross-link and slide one MT relative to another (5–17). Sequence analysis indicates that all members of the kinesin-14 subfamily are dimeric, yet the structural organization of kinesin-14 motors differs from the N-terminal processive kinesins. The kinesin-14s exhibit C-terminal motor domains connected by an N-terminal continuous coiled-coil stalk with an N-terminal ATP-independent MT binding site (7, 18–22). And although most of the kinesin-14s are homodimeric, some yeast species, including *Saccharomyces cerevisiae* and *Candida glabrata*, contain heterodimeric kinesin-14s (13, 14, 19). The conventional hypothesis for homodimeric kinesin-14 force generation proposed that only one motor head interacts with the MT and only one ATP turnover is required to complete the powerstroke (Fig. S1*A*) (10, 12). In contrast, our presteady-state kinetics (9, 23, 24) and the results of Kocik et al. (25) concluded that both Ncd heads were required for Ncd force generation and also documented cooperative interactions between the Ncd heads during ATP-promoted MT interactions. The scheme in Fig. S1*B* accounted for these results and proposed that both Ncd heads interact with the microtubule, and two ATP turnovers are required (24).

Through our recent studies on *S. cerevisiae* Kar3Vik1 and Kar3Cik1, we discovered novel properties of these yeast kinesin-14s that challenged the earlier models of how kinesin-14s generate force for their cellular functions (13, 15, 26–28). The C-terminal globular domain of Vik1 exhibits the structure of a kinesin motor domain (MD), yet Vik1 as well as Cik1 lack a nucleotide-binding site (13, 26). Because the C-terminal domain of Vik1 binds MTs independently of Kar3 and with high affinity (26), it was designated the Vik1 motor homology domain (MHD). A series of site-directed cross-links at the base of the coiled coil near the motor heads of Kar3Vik1 were introduced, and motility assays indicated that both the Kar3MD and Vik1MHD must interact with the MT lattice to generate sustained MT gliding, yet significant unwinding of the coiled coil was not required (>10 Å but <20 Å) (13). This series of experiments led to the proposal that Kar3Vik1 binds the MT lattice on adjacent MT protofilaments rather than a single protofilament in a head-to-tail fashion because such a small degree of unwinding of the coiled coil would not allow the 8-nm separation required for the two-head bound state. Indeed, high-resolution unidirectional metal shadowing, which strongly emphasizes the surface features when viewed by EM, also captured this mode of MT binding in the presence of ADP. The unidirectional metal shadowing experiments were repeated for Kar3Cik1 and Ncd, and both exhibited this noncanonical MT binding configuration, suggesting that the adjacent MT protofilament binding configuration may be

Significance

Kinesin molecular motors couple ATP turnover to force production to generate microtubule-based movement and microtubule dynamics. Kinesin-14s are unique in that they are nonprocessive, bind to adjacent microtubule protofilaments rather than step along a single protofilament as observed for processive kinesins, and use a powerstroke mechanism to slide microtubules. Earlier studies proposed that only one head of the Ncd dimer interacts with the microtubule to drive the ATP-promoted powerstroke and therefore only one ATP turnover was required. The results presented here challenge the one head/one ATP turnover hypothesis and define a common pathway for Kar3Vik1, Kar3Cik1, and Ncd. These findings are significant because they reveal that the key principles for force generation by kinesin-14s are conserved from yeast to higher eukaryotes.

Author contributions: P.Z., W.D., J.H., and S.P.G. designed research; P.Z. and W.D. performed research; P.Z., W.D., J.H., and S.P.G. analyzed data; and P.Z., W.D., J.H., and S.P.G. wrote the paper.

This article is a PNAS Direct Submission.

[1]P.Z. and W.D. contributed equally to this work.

[2]To whom correspondence may be addressed. Email: sgilbert@rpi.edu or hahnj@rpi.edu.

This article contains supporting information online at www.pnas.org/lookup/suppl/doi:10.1073/pnas.1505531112/-/DCSupplemental.

characteristic of kinesin-14s in general and not specific to Kar3Vik1 and/or Kar3Cik1 (15).

CryoEM and subsequent helical reconstruction of the MT complexes of Kar3Vik1 and Kar3Cik1 at different nucleotide states captured the same nucleotide-dependent powerstroke intermediates as reported for Ncd (10–13, 15). Apyrase was used to generate the nucleotide-free prepowerstroke state (Fig. 1, E4), and AMPPNP, the nonhydrolyzable ATP analog, revealed a postpowerstroke intermediate in which the coiled-coil stalk was rotated ∼70 degrees toward the MT minus end (Fig. 1, E5). Because Kar3Vik1, Kar3Cik1, and Ncd share common structural similarities at distinct nucleotide states, we hypothesized that Ncd must use the same series of structural transitions for force production even though both Ncd motor heads are catalytic.

Therefore, a series of experiments were pursued to test the proposed scheme presented in Fig. 1 and to validate or rule out two earlier models (Fig. S1). The following assumptions were made based on earlier studies (9, 13, 23, 24, 26–28): (*i*) In solution, homodimeric Ncd exhibits an asymmetry in which one head holds ADP tightly bound while the partner head holds ADP weakly (E0) (24). (*ii*) MT collision is followed by rapid ADP release (E0–E1) (24). (*iii*) By analogy to Kar3Vik1, the head that initially collides with the MT (E1) binds α-tubulin in a noncanonical MT binding configuration and is rotated relative to its partner head that binds β-tubulin (E4) (13, 26). (*iv*) ATP binding at the first head (E2) promotes MT binding of the partner head followed by ADP release to generate the prepowerstroke intermediate (E2–E4) (24) (*v*) ATP binding at head 2 generates the postpowerstroke intermediate with the coiled-coil stalk rotated ∼70° (E5) (10, 12). (*vi*) Motor detachment from the MT occurs after the ATP-promoted powerstroke and after ATP hydrolysis (E5–E6) (23). (*vii*) There are two ATP binding and hydrolysis events to generate one powerstroke (9, 24). (*viii*) The powerstroke occurs later in the scheme and can only occur upon ATP binding to the Ncd head bound to β-tubulin (10, 12). (*ix*) Ncd•ADP•P_i rather than Ncd•ADP may be the weakest MT binding state for at least one of the Ncd heads based on earlier MT•Ncd cosedimentation studies (E3 and/or E6) (23).

Results

Two ATP Turnover Events Are Required Per Powerstroke. Before pursuing new experiments to test the mechanism in Fig. 1, the pulse-chase and acid-quench presteady-state kinetics experiments were repeated to evaluate whether two ATP binding and hydrolysis events were required before Ncd detachment from the MT as proposed previously (9, 24). For these experiments, the previously characterized N-terminal truncation of Ncd MC1 was used (9, 23, 24, 29).

The results presented in Figs. S2 and S3 and Table S1 show conclusively that two ATP turnovers occurred before Ncd detachment from the MT with the interpretation that there was one ATP turnover per Ncd head. These results rule out the model in Fig. S1*A*, in which only one Ncd head interacts with the MT and one ATP binding event drives the rotation for the powerstroke (10, 12). However, these results are consistent with the earlier scheme proposed by Foster et al. (24) (Fig. S1*B*).

The Foster et al. model (24) (Fig. S1*B*) was based on the assumption that the Ncd would have an ATPase mechanochemical cycle more similar to that of kinesin-1 in that there was a MT two-head bound state with one true step, and the second ATP turnover was required to detach Ncd from the MT. Note that this model was proposed before the publications that supported the Ncd lever-arm rotation model (10–12). With the more recent insights from studies on Kar3Cik1 and Kar3Vik1, a fresh perspective was needed to test these models, and the next series of experiments were designed to reveal transient intermediates that were not captured previously by mechanistic or structural studies.

A Slow Structural Transition Is Required Before ATP Binding. A new experiment was designed to mimic the reaction condition at the beginning of the cycle where Ncd collides with the MT followed by ADP release and subsequent ATP binding at head 1 (Fig. 1, E0–E2). For Kar3Cik1 and Kar3Vik1, this strategy was necessary to capture the transient E1 state in which the MHD collided with the MT first (27, 28). For these experiments, 10 μM Ncd•ADP was rapidly mixed in the stopped-flow instrument with 40 μM MTs plus the fluorescent ATP analog 2′-(3′)-*O*-(*N*-methylanthraniloyl) ATP (mantATP). At these concentrations (final: 5 μM Ncd•ADP, 20 μM MTs), Ncd MT association is fast and occurs before mantATP binding (Table S1). Fig. 2*A* shows representative transients at 0.5–5 μM mantATP, and Fig. 2*B* presents the observed rates of mantATP binding as a function of mantATP concentration. A hyperbolic function plus a *y*-intercept was fit to the data and provided the maximum rate constant of 4.4 s^{-1}. Previous experiments at similar conditions measured the rate constant of mantATP binding to the preformed MT•Ncd complex at 2.3 $\mu M^{-1}{\cdot}s^{-1}$, or for example 35 s^{-1} at 15 μM mantATP (9). Furthermore, mantADP release from the active site of the first Ncd head upon MT collision was 17.8 s^{-1} (24) (Table S1). Therefore, these results are consistent with a slow conformational change that occurs after MT collision followed by fast ADP release and before ATP binding. We propose that the experimental design in Fig. 2 has captured the slow conformational change that occurs after MT collision to form the transient E1 intermediate that is poised to bind ATP.

If a slow conformational change were required to form the E1 intermediate poised for ATP binding, then this step can be bypassed by preforming the MT•Ncd intermediate. This strategy was used to measure the kinetics of ATP binding and ATP hydrolysis revealing that both were fast events (Figs. S2 and S3) and to measure the kinetics for phosphate release (Fig. 3 *A*–*C*).

The Intrinsic Rate Constant of Phosphate Release Is Fast. To measure the kinetics of phosphate release, the Martin Webb fluorescently labeled phosphate binding protein (MDCC-PBP) assay was used (30, 31). The MT•Ncd complex was preformed, MDCC-PBP was added (final concentrations: 2.5 μM Ncd•ADP, 20 μM MTs, 10 μM MDCC-PBP), and then the reactants were rapidly mixed with ATP plus KCl. The additional salt in the ATP syringe does not affect the first ATP turnover but limits additional ATP turnovers by weakening the binding of the second motor head to the MT (31). ATP binding and hydrolysis occur rapidly at the active site, followed by phosphate release. The phosphate

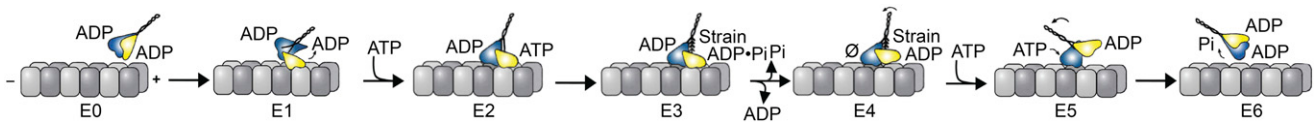

Fig. 1. Proposed Ncd powerstroke mechanism. Homodimeric Ncd in solution is asymmetric with one head holding ADP tightly bound and the other head with ADP weakly bound. The cycle begins with MT collision of head 1 (low ADP affinity, yellow) followed by rapid ADP release to form intermediate E1. ATP binds to head 1, promoting the association of head 2 (blue head) to the adjacent MT protofilament to form the E2 transient intermediate. ATP hydrolysis is required at head 1 for release of ADP from head 2. This transition results in the prepowerstroke E4 intermediate with head 2 tightly bound and nucleotide-free, and head 1 detached from the MT. ATP binding at head 2 drives the ∼70° rotation of the coiled-coil stalk toward the MT minus end forming the E5, postpowerstroke state. ATP hydrolysis at head 2 leads to Ncd detachment from the MT (E6), followed by its rapid transition to the E0 intermediate poised for MT binding.

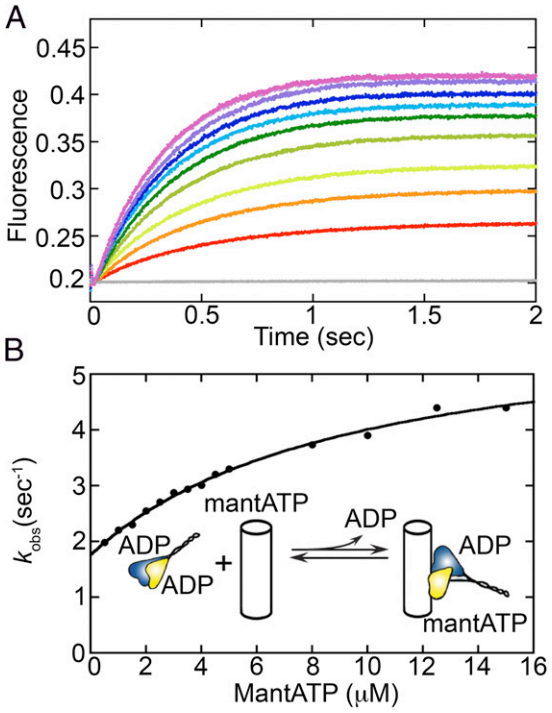

Fig. 2. MantATP binding following MT•Ncd association. Ncd•ADP was rapidly mixed in the stopped-flow instrument with MTs plus increasing concentrations of mantATP. Final concentrations: 5 μM Ncd•ADP sites, 20 μM MTs, and 0.5–15 μM mantATP. (*A*) Transients are shown from low to high concentrations: 0, 0.5, 1, 1.5, 2, 2.5, 3, 3.5, 4, 4.5, and 5 μM mantATP, and a single exponential function was fit to each. (*B*) The observed rates of the exponential phase of mantATP binding were plotted as a function of mantATP concentration. A hyperbolic function plus a *y*-intercept was fit to the data, which provided the maximum rate constant of 4.4 ± 0.2 s^{-1}, k_{off} of 1.8 ± 0.1 s^{-1}, and $K_{1/2,mantATP}$ of 9.4 ± 1.4 μM. (*Inset*) Illustration of experimental design.

released to solution was bound rapidly and tightly by MDCC-PBP, eliciting an increase in fluorescence that can be quantified (Fig. 3). Fig. 3*A* shows representative transients at varying ATP concentrations. These transients are biphasic and display a lag, attributed to ATP binding and ATP hydrolysis. The observed rate of the initial exponential phase of each transient was plotted as a function of ATP concentration (Fig. 3*B*), and the hyperbolic fit to the data provides the maximum rate constant of phosphate release at 14.3 s^{-1}.

A phosphate standard curve (Fig. 3*C*, *Inset*) was used for each transient to convert the exponential amplitude associated with phosphate release in units of relative fluorescence to units of phosphate concentration. The hyperbolic fit to the data (Fig. 3*C*) revealed a maximum amplitude of 1.1 μM phosphate for 2.5-μM Ncd sites, indicating that the phosphate release data represent 44% of the sites. These results are consistent with the interpretation that the experimental design for Fig. 3 *A–C* captured the intrinsic rate constant of phosphate release from head 1 that occurs after step E3 due to the additional salt added in the ATP syringe for this experiment.

The Slow Structural Transition After MT Collision Can Also Be Captured by Phosphate Release Kinetics. If a slow conformational change were required for ATP binding, then the rate constant of phosphate release would also be slow because phosphate release occurs after ATP binding and ATP hydrolysis. Fig. 3 *D–F* shows the results in which the kinetics of phosphate release were measured from head 1 and head 2. This experimental design mimicked the start of the cycle as in Fig. 2 where 10 μM Ncd•ADP plus 15 μM MDCC-PBP were rapidly mixed in the stopped-flow instrument with 40 μM MTs with varying ATP (final: 5 μM Ncd•ADP, 7.5 μM MDCC-PBP, 20 μM MTs). Note that no additional KCl was added to the ATP syringe, and at the conditions of this experiment, Ncd•ADP collision with the MT occurs before ATP binding. Once ATP binding and hydrolysis occur, phosphate is released from the active site. MDCC-PBP rapidly binds the free phosphate released to the solution resulting in an increase in fluorescence. Fig. 3*D* shows representative transients, and the observed rate of the initial exponential phase associated with phosphate release was plotted as a function of ATP concentration (Fig. 3*E*). The hyperbolic fit to the data provided a maximum rate constant for phosphate release at 2.9 s^{-1}, consistent with the interpretation that a slow conformational change must occur before ATP binding to limit the rate of phosphate release.

The phosphate standard curve in Fig. 3*F* was used to convert the exponential amplitude associated with phosphate release in units of relative fluorescence to units of phosphate concentration, and these data were plotted as a function of ATP concentration. The amplitude data can be correlated with the concentration of Ncd sites (5 μM Ncd•ADP) that bind and hydrolyze ATP, followed by phosphate release. The maximum amplitude at 5.7 μM (1.1 P_i/Ncd site) is consistent with the interpretation that two ATP turnover events were required before Ncd detachment from the MT (Fig. 1, E0–E6).

The phosphate release kinetics (Fig. 3), in combination with the results from Fig. 2, place a slow step early in the scheme after MT collision and before ATP binding. The experimental design for Fig. 3 *A–C* captured phosphate release after one ATP turnover from head 1 and revealed that phosphate release is intrinsically a fast step at 14.3 s^{-1}.

Computational Modeling of the Proposed Mechanism. To test the validity of the proposed mechanism in Fig. 1, we performed computational modeling. The transients in Fig. 2*A* were fit to a single exponential equation. However, from a modeling perspective, this type of model is the analytical solution of a certain class of dynamic systems described by a set of linear ordinary differential equations (ODEs). Though the exponential equation fits the experimental data with a very good degree of accuracy, it has to be refit for different experimental conditions potentially due to the existence of nonlinearity in the powerstroke process, which makes the estimated parameter values inconsistent and difficult to interpret. Therefore, a first principles-based model represented by nonlinear ODEs (32) was developed with the goal to capture the dynamics of the Ncd powerstroke process (shown in Fig. 1) for a variety of different initial concentrations of mantATP (Fig. 2). The model is described in more detail below and summarized in Fig. 4.

E0 → E1. The start of the Ncd powerstroke consists of three separate steps: (*i*) Ncd in solution with ADP on both heads, Ncd•ADP•ADP (denoted as X_1 here) collides with a MT and forms the MT•Ncd•ADP•ADP collision complex (denoted as N_1): $X_1 \rightleftharpoons N_1$. Because this step is fast and reversible, the reaction will quickly reach an equilibrium where the ratio of $[N_1]$ to $[X_1]$, where [ ] represents the concentration, is a constant denoted by K_1. (*ii*) After MT collision, ADP on the first Ncd head is released to form the MT•Ncd•Ø•ADP intermediate (denoted as N_2). Here, Ø represents an empty active site: $N_1 \rightleftharpoons N_2$. This step is fast and reversible, i.e., it will quickly reach equilibrium, thus the ratio of $[N_2]$ and $[N_1]$ is a constant denoted by K_2. (*iii*) The MT•Ncd•Ø•ADP intermediate undergoes a conformational change and forms the MT•Ncd*•Ø•ADP intermediate (denoted as X_2). Here, * represents the complex after the conformational change has taken place: $N_2 \rightleftharpoons X_2$. When writing the rate expression, the constants K_1 and K_2 can be combined as part of the overall reaction rate to yield the following expression:

$$X_1 \underset{k_{-1}}{\overset{k_1}{\rightleftharpoons}} X_2, \qquad [1]$$

where k_1 and k_{-1} represent the reaction rates where the information from the three steps above are combined. Eq. **1** describes

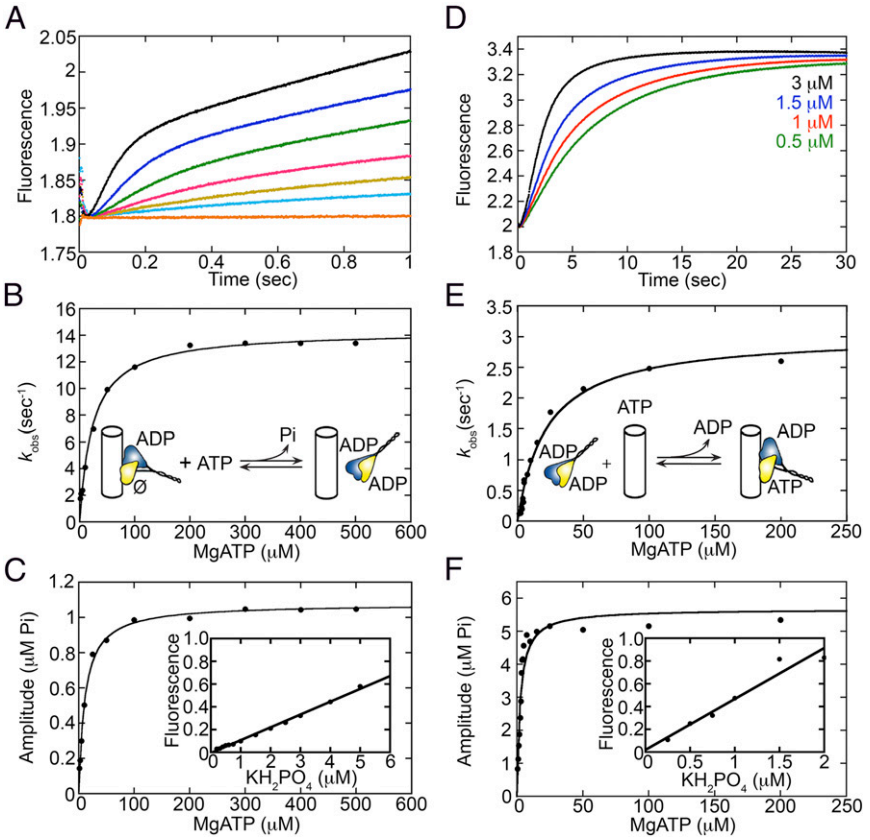

Fig. 3. Phosphate release. (*A–C*) Phosphate release from the MT•Ncd complex. The MT•Ncd complex was preformed, and subsequently the MT•Ncd complex plus MDCC-PBP were rapidly mixed in the stopped-flow instrument with the increasing concentrations of MgATP plus 200 mM KCl (syringe concentration). The fluorescence enhancement of MDCC-PBP upon binding inorganic phosphate (P_i) was monitored. Final concentrations: 2.5 μM Ncd•ADP sites, 20 μM MTs, 10 μM MDCC-PBP, 0.025 U/mL PNPase, 75 μM MEG, and 1.25–500 μM MgATP. (*A*) Representative transients of P_i product release from Ncd following ATP hydrolysis are shown from low to high concentrations: 0, 1.25, 2.5, 5, 10, 25, and 100 μM of MgATP. (*B*) The observed exponential rate of P_i release from each transient was plotted as a function of MgATP concentration, and the hyperbolic fit to the data provided $k_{max} = 14.3 \pm 0.3\ s^{-1}$ and $K_{1/2,ATP} = 23.3 \pm 2.3$ μM. (*Inset*) Experimental design. (*C*) The amplitude (A_0) of the initial exponential phase of each transient was plotted as a function of MgATP concentration, and the hyperbolic fit to the data provided the maximum amplitude $A_{0,max} = 1.1 \pm 0.01$ μM (~44% Ncd sites). (*Inset*) Phosphate standard curve used to convert the relative fluorescence in volts to micromolar P_i. (*D–F*) Phosphate release following MT•Ncd association. Ncd•ADP plus MDCC-PBP were rapidly mixed with MTs in the presence of increasing concentrations of MgATP, and the fluorescence enhancement was monitored. Final concentrations: 5 μM Ncd•ADP, 20 μM MTs, 7.5 μM MDCC-PBP, 0.025 U/mL PNPase, 75 μM MEG, and 0.5–500 μM MgATP. (*D*) Representative transients of P_i product release from Ncd following ATP hydrolysis. (*E*) The observed exponential rate of P_i release was plotted as a function of MgATP concentration, and the hyperbolic fit to the data provided the maximum rate constant for P_i release at $2.9 \pm 0.1\ s^{-1}$ with $K_{1/2,ATP} = 16 \pm 0.97$ μM. (*Inset*) Illustration of the experimental design. (*F*) The amplitude of the initial exponential phase of each transient was plotted as a function of MgATP concentration, and the hyperbolic fit to the data provided $A_{0,max} = 5.7 \pm 0.25$ μM (~1.1 P_i/Ncd site). (*Inset*) Phosphate standard curve used to convert the relative fluorescence in volts to micromolar P_i.

the process before the binding of mantATP to the first head of Ncd.

E1 → E2. MantATP (denoted as M) binds the first head and forms MT•Ncd*•mantATP•ADP (denoted as X_3). A fluorescence signal is released during this step. The model describing this step is given by

$$X_2 + M \underset{k_{-2}}{\overset{k_2}{\rightleftharpoons}} X_3, \qquad [2]$$

where k_2 is the binding rate of mantATP to the first head and k_{-2} is the mantATP dissociation rate constant.

E2 → E3. MantATP hydrolysis at the first head is fast and nonreversible.

E3 → E4. MantATP binding at the first head signals the second Ncd head to bind to the MT and release ADP. MantATP hydrolysis forms the MT•Ncd*•mantADP•P_i•Ø intermediate (denoted as X_4) in this process. The Ncd*•mantADP•P_i head may detach from the MT followed by rapid phosphate release or phosphate release may occur first followed by detachment as Ncd*•mantADP. This coupled event is slow and weakly reversible. Therefore, the steps from E2 to E4 can be combined and modeled as follows:

$$X_3 \overset{k_3}{\rightarrow} X_4, \qquad [3]$$

where k_3 is a reaction rate incorporating the entire process after the binding of mantATP to the first head and before mantATP binding to the second head. It should be noted that the fluorescence signal still exists when mantADP is bound to the first head; however, the intensity may potentially change.

E4 → E5. MantATP binds to the second head (denoted as M) to form the MT•Ncd*•mantADP•mantATP intermediate. MantATP binding to the second head promotes the rotation of the coiled-coil stalk, i.e., the powerstroke, and these coupled reactions are fast.

E5 → E6. MantATP on the second head is hydrolyzed, and then P_i is released to form the MT•Ncd*•mantADP•mantADP intermediate (denoted as X_5). This process is fast and nonreversible. Because the fluorescence signal still exists after mantATP hydrolysis, although the change of intensity is unknown, the processes from E4 to E6 are combined and modeled as follows:

$$X_4 + M \overset{k_4}{\rightarrow} X_5, \qquad [4]$$

where k_4 represents the reaction rate, including the process of mantATP binding to the second head and the subsequent hydrolysis.

Parameter Estimation. The initial concentration of mantATP is different in each of the nine experiments (Fig. 2*A*). Data obtained from experiments 1, 3, 5, 7, and 9 were used for model fitting via parameter estimation, and data obtained from experiments 2, 4, 6, and 8 were used to further validate model prediction accuracy (Fig. 4). The method used for estimation is explained in detail in *SI Materials and Methods*. The estimated parameters are listed in Fig. 4*C*, and the simulation results using the estimated parameters are shown in Fig. 4*D*. It can be seen

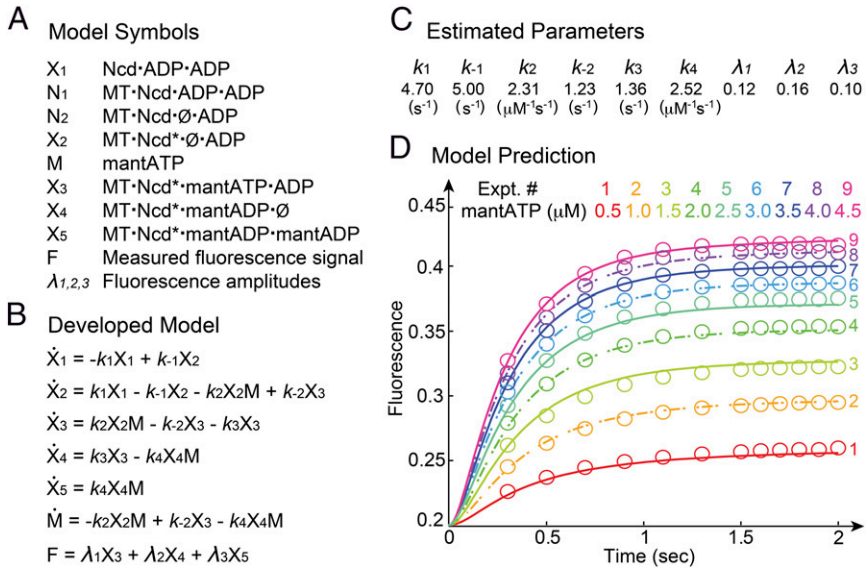

Fig. 4. Modeling of the proposed mechanism. (*A*) Model components and the corresponding symbols. (*B*) The developed first principles-based model describing the steps given in Eqs. **1–4** is written as a set of ODEs. (*C*) Unknown parameters are estimated for the model using data obtained from experiments 1, 3, 5, 7, and 9 (Fig. 2*A*). (*D*) Model predictions using estimated parameters. Circles are experimental data under different initial concentrations of mantATP (Fig. 2*A*). Solid lines are model predictions for the cases where experimental data were used for training. Dashed lines are the model predictions where the experimental data were not used for training but for validation.

that the results obtained for both the training and, more importantly, the validation sets are in good agreement with the experimental data.

Several conclusions can be drawn from the estimated parameters. First, parameter k_1 has a value of 4.70 s^{-1}, which is consistent with the assumption that the conformational change at the start of the cycle is a slow step. Second, parameter k_2 has a value of 2.31 $\mu M^{-1}{\cdot}s^{-1}$, which is within the commonly assumed range of the ATP binding rate of 2–3 $\mu M^{-1}{\cdot}s^{-1}$ and which was experimentally measured at 2.3 $\mu M^{-1}{\cdot}s^{-1}$ (Table S1). Third, the parameter k_3 has a value of 1.36 s^{-1}, which is consistent with the experimentally determined rate constant of mantADP release from the second head at 1.4 s^{-1} and the steady-state ATPase k_{cat} measured at 2.1 s^{-1} (Table S1). Fourth, parameter k_4 has a value of 2.52 $\mu M^{-1}{\cdot}s^{-1}$, which is within the commonly assumed range of ATP binding rates of 2–3 $\mu M^{-1}{\cdot}s^{-1}$.

Discussion

Earlier studies suggested that only one head of Ncd interacted with the MT at a time (Fig. S1*A*), and the data were based on cryoEM studies that failed to capture a stable intermediate with both Ncd heads bound to the MT (10, 12). MT gliding experiments were performed in which Ncd heterodimers with only one motor head promoted wild-type rates of gliding, and the steady-state ATPase scaled with the concentration of motor heads (12). These results appeared at the time to provide definitive evidence to support the one head/one ATP turnover powerstroke model. However, these studies can now be interpreted in the context of multiple single Ncd heads driving normal MT gliding.

The studies with Kar3Vik1 and Kar3Cik1 provided insights for another potential model for Ncd not previously considered because the assumption at the time was that an Ncd homodimer would bind to the MT in a head-to-tail fashion on a single MT protofilament (Fig. S1*B*). The publications documenting that Kar3Vik1, Kar3Cik1, and Ncd bind to adjacent protofilaments on the MT lattice (13, 15) in combination with similarity in their prepowerstroke and postpowerstroke intermediates resulted in the experiments reported here to ask if homodimeric Ncd with two ATP binding sites can modulate MT interactions much like Kar3Vik1 and Kar3Cik1. The scheme in Fig. 1 guided the experiments and led to new insights.

The Initial Steps from E0 to E4 to Form the Prepowerstroke Intermediate. For Ncd, one head holds ADP tightly and the partner head holds ADP weakly (24); therefore, there is an asymmetry in Ncd reminiscent of Kar3Vik1 and Kar3Cik1. We propose based on earlier work that the initial collision with the MT occurs by the head that holds ADP weakly resulting in rapid ADP release at 17.8 s^{-1} (Fig. 1, E0–E1; Table S1) (24). The results in Fig. 2 and Fig. 3 *D–F* indicate that a slow conformational change at 4.4 s^{-1} must occur after MT collision to generate the transient E1 intermediate poised for ATP binding. ATP binding occurs rapidly at 2.3 $\mu M^{-1}{\cdot}s^{-1}$ (Table S1) (9), and ATP binding at head 1 is required for head 2 to bind to the MT to form the E3 intermediate (24). However, in experiments designed to look at mantADP release from head 2 specifically (E3–E4), ATP binding at head 1 was not sufficient for head 2 to release mantADP upon MT association (24). Rather, ATP hydrolysis was also required to generate the E4 prepowerstroke intermediate (figure 3 in ref. 24). In other experiments designed to measure mantADP release from both heads upon MT collision by inclusion of ATP in the MT syringe (Fig. 1, E0–E4), the transients were biphasic with an initial fast rate of mantADP at 14.2 s^{-1}, followed by a second slow phase of mantADP release at 1.85 s^{-1} (Fig. S4; Table S1). These results are consistent with earlier studies as well as the parameters obtained from the computational modeling (Fig. 4).

The Steps from E4 to E6 to Complete the Powerstroke. The experiments to measure the steps from E4 to E6 were performed previously (9, 23, 24), and we propose that head 2 is bound to β-tubulin and nucleotide-free. The pulse-chase experiments (Fig. S2) revealed a rapid ATP-promoted isomerization at 81 s^{-1}, which has been interpreted to represent the structural transitions required to form the intermediate poised for ATP hydrolysis (27, 28). This postpowerstroke intermediate was captured by cryoEM using the nonhydrolyzable ATP analog, AMPPNP (10, 12). Acid-quench experiments show that ATP hydrolysis was rapid at 26 s^{-1} (Fig. S3; Table S1) (9, 24) and was required for Ncd to detach from the MT (E6) (24). Interestingly, ATP hydrolysis for Kar3-Cik1 and Kar3Vik1 were also measured at 26 s^{-1} (27, 28), reflecting the similarity of residues at the pivot point for the coiled-coil stalk rotation and the active site residue configuration for ATP hydrolysis. The presteady-state kinetics performed previously measured the dissociation step at 12–14 s^{-1} (Table S1) (23, 24), and it is proposed that after detachment from the MT, the Ncd E6 intermediate returns to the E0 state, poised to rebind to the MT.

The Ncd•ADP•P_i State. For kinesins, the data suggest that the ADP state is the weakest MT bound state. In fact, most kinesins, including Ncd, are purified with ADP bound at the active sites. However, when the equilibrium MT Ncd cosedimentation

experiments were performed, ADP generated an Ncd intermediate that remained bound to the MT (23). The interpretation was that because of the cooperativity, ADP remained bound to the head detached from the MT with the MT-bound Ncd head, nucleotide-free. In fact, the only state that was weakly bound to the MT was generated by the addition of 2 mM ADP plus potassium phosphate. These data were plotted as the fraction of Ncd partitioning to the supernatant as a function of potassium phosphate concentration. Rather than showing a hyperbolic binding curve, a sigmoidal binding curve was observed, indicating cooperativity between the two Ncd sites (23). Although it is not known whether detachment of head 1 occurs as an ADP•P_i intermediate or whether phosphate release occurs first at 14.3 s^{-1} followed by detachment as the ADP state (E3–E4), it is reasonable to propose, based on the cosedimentation results and the noncanonical MT binding configuration, that head 1 detaches from the MT directly after ATP hydrolysis as the ADP•P_i state. In contrast, Ncd at E6 may detach as the Ncd•ADP state because the MT•Ncd E5 intermediate is bound to β-tubulin rather than α-tubulin. Regardless, the data indicate that Ncd dissociation from the MT and phosphate release are coupled reactions with one occurring rapidly and the other occurring more slowly, and experimentally only the slow step can be observed.

The Computational Model. The results in Fig. 4 provide further evidence to support the proposed mechanism in Fig. 1. The two most important parameters from the modeling were the prediction of a 4.7 s^{-1} structural transition that occurs after MT collision and before ATP binding, and a slow step of 1.37 s^{-1} associated with mantADP release and similar to the experimentally determined rate constant of mantADP release at 1.4 s^{-1} from the second head and steady-state ATP turnover at 2.1 s^{-1} (Table S1). In fact, it is remarkable that the computational model fit the mantATP binding experimental data so well.

The computational model was also used to test the validity of the Foster et al. (24) scheme in Fig. S1*B*, which lacks the slow conformational change at 4.7 s^{-1} early in the cycle. The model predictions for the Foster et al. (24) scheme do not fit the data well, because almost all of the transients and several of the steady states for intermediate mantATP concentrations are poorly predicted by the model. Also, the fits lack the initial lag phase revealed by the experiments in Fig. 2 and captured by the computational model presented in this work in Fig. 4.

In conclusion, the studies with *S. cerevisiae* Kar3Vik1 and Kar3Cik1 provided new insights and challenged us to ask experimentally whether homodimeric Ncd behaves more like Kar3Vik1 and Kar3Cik1 than the processive kinesins. The significance of the findings reported here is the conclusion that the key principles for force generation by kinesin-14s are evolutionarily conserved from yeast to higher eukaryotes. In addition, the results show conclusively that for Ncd, two ATP turnovers are required to generate a single powerstroke displacement or step in contrast to conventional myosin II (33) and the processive myosins and kinesins, which require only a single ATP turnover for each step (34, 35). Therefore, this study implicates the homodimeric kinesin-14s as a novel class of molecular motors where two ATP turnover events are required for each powerstroke-driven microtubule displacement or step.

Materials and Methods

Errors are reported as ±SEM. A complete description of the plasmids, proteins, and methods used is provided in *SI Materials and Methods*.

ACKNOWLEDGMENTS. This work was supported by NIH Grant 2R37GM54141 (to S.P.G.), National Science Foundation Chemical, Bioengineering, Environmental, and Transport Systems Grant 0941313, and American Chemical Society Petroleum Research Fund Grant 50978-ND9 (to J.H.).

1. Endow SA, Henikoff S, Soler-Niedziela L (1990) Mediation of meiotic and early mitotic chromosome segregation in *Drosophila* by a protein related to kinesin. *Nature* 345(6270):81–83.
2. McDonald HB, Goldstein LSB (1990) Identification and characterization of a gene encoding a kinesin-like protein in *Drosophila*. *Cell* 61(6):991–1000.
3. Mountain V, et al. (1999) The kinesin-related protein, HSET, opposes the activity of Eg5 and cross-links microtubules in the mammalian mitotic spindle. *J Cell Biol* 147(2): 351–366.
4. Sharp DJ, Yu KR, Sisson JC, Sullivan W, Scholey JM (1999) Antagonistic microtubule-sliding motors position mitotic centrosomes in *Drosophila* early embryos. *Nat Cell Biol* 1(1):51–54.
5. McDonald HB, Stewart RJ, Goldstein LSB (1990) The kinesin-like Ncd protein of *Drosophila* is a minus end-directed microtubule motor. *Cell* 63(6):1159–1165.
6. Walker RA, Salmon ED, Endow SA (1990) The *Drosophila* claret segregation protein is a minus-end directed motor molecule. *Nature* 347(6295):780–782.
7. Sablin EP, et al. (1998) Direction determination in the minus-end-directed kinesin motor Ncd. *Nature* 395(6704):813–816.
8. Pechatnikova E, Taylor EW (1999) Kinetics processivity and the direction of motion of Ncd. *Biophys J* 77(2):1003–1016.
9. Foster KA, Gilbert SP (2000) Kinetic studies of dimeric Ncd: Evidence that Ncd is not processive. *Biochemistry* 39(7):1784–1791.
10. Wendt TG, et al. (2002) Microscopic evidence for a minus-end-directed power stroke in the kinesin motor Ncd. *EMBO J* 21(22):5969–5978.
11. Yun M, et al. (2003) Rotation of the stalk/neck and one head in a new crystal structure of the kinesin motor protein, Ncd. *EMBO J* 22(20):5382–5389.
12. Endres NF, Yoshioka C, Milligan RA, Vale RD (2006) A lever-arm rotation drives motility of the minus-end-directed kinesin Ncd. *Nature* 439(7078):875–878.
13. Rank KC, et al. (2012) Kar3Vik1, a member of the kinesin-14 superfamily, shows a novel kinesin microtubule binding pattern. *J Cell Biol* 197(7):957–970.
14. Duan D, et al. (2012) Neck rotation and neck mimic docking in the noncatalytic Kar3-associated protein Vik1. *J Biol Chem* 287(48):40292–40301.
15. Gonzalez MA, et al. (2013) Common mechanistic themes for the powerstroke of kinesin-14 motors. *J Struct Biol* 184(2):335–344.
16. Jana B, Hyeon C, Onuchic JN (2012) The origin of minus-end directionality and mechanochemistry of Ncd motors. *PLOS Comput Biol* 8(11):e1002783.
17. Kull FJ, Endow SA (2013) Force generation by kinesin and myosin cytoskeletal motor proteins. *J Cell Sci* 126(Pt 1):9–19.
18. Meluh PB, Rose MD (1990) KAR3, a kinesin-related gene required for yeast nuclear fusion. *Cell* 60(6):1029–1041.
19. Barrett JG, Manning BD, Snyder M (2000) The Kar3p kinesin-related protein forms a novel heterodimeric structure with its associated protein Cik1p. *Mol Biol Cell* 11(7): 2373–2385.
20. Manning BD, Snyder M (2000) Drivers and passengers wanted! The role of kinesin-associated proteins. *Trends Cell Biol* 10(7):281–289.
21. Karabay A, Walker RA (1999) Identification of microtubule binding sites in the Ncd tail domain. *Biochemistry* 38(6):1838–1849.
22. Fink G, et al. (2009) The mitotic kinesin-14 Ncd drives directional microtubule-microtubule sliding. *Nat Cell Biol* 11(6):717–723.
23. Foster KA, Correia JJ, Gilbert SP (1998) Equilibrium binding studies of non-claret disjunctional protein (Ncd) reveal cooperative interactions between the motor domains. *J Biol Chem* 273(52):35307–35318.
24. Foster KA, Mackey AT, Gilbert SP (2001) A mechanistic model for Ncd directionality. *J Biol Chem* 276(22):19259–19266.
25. Kocik E, Skowronek KJ, Kasprzak AA (2009) Interactions between subunits in heterodimeric Ncd molecules. *J Biol Chem* 284(51):35735–35745.
26. Allingham JS, Sproul LR, Rayment I, Gilbert SP (2007) Vik1 modulates microtubule-Kar3 interactions through a motor domain that lacks an active site. *Cell* 128(6): 1161–1172.
27. Chen CJ, Porche K, Rayment I, Gilbert SP (2012) The ATPase pathway that drives the kinesin-14 Kar3Vik1 powerstroke. *J Biol Chem* 287(44):36673–36682.
28. Chen CJ, Rayment I, Gilbert SP (2011) Kinesin Kar3Cik1 ATPase pathway for microtubule cross-linking. *J Biol Chem* 286(33):29261–29272.
29. Chandra R, Endow SA, Salmon ED (1993) An N-terminal truncation of the ncd motor protein supports diffusional movement of microtubules in motility assays. *J Cell Sci* 104(Pt 3):899–906.
30. Brune M, Hunter JL, Corrie JET, Webb MR (1994) Direct, real-time measurement of rapid inorganic phosphate release using a novel fluorescent probe and its application to actomyosin subfragment 1 ATPase. *Biochemistry* 33(27):8262–8271.
31. Klumpp LM, Hoenger A, Gilbert SP (2004) Kinesin's second step. *Proc Natl Acad Sci USA* 101(10):3444–3449.
32. Singh A, Jayaraman A, Hahn J (2006) Modeling regulatory mechanisms in IL-6 signal transduction in hepatocytes. *Biotechnol Bioeng* 95(5):850–862.
33. Geeves MA, Holmes KC (1999) Structural mechanism of muscle contraction. *Annu Rev Biochem* 68:687–728.
34. Sun Y, Goldman YE (2011) Lever-arm mechanics of processive myosins. *Biophys J* 101(1):1–11.
35. Clancy BE, Behnke-Parks WM, Andreasson JO, Rosenfeld SS, Block SM (2011) A universal pathway for kinesin stepping. *Nat Struct Mol Biol* 18(9):1020–1027.